Chiral single photons from deterministic quantum emitter arrays via proximity coupling to van der Waals ferromagnets

2D Materials

OPEN ACCESS

RECEIVED
28 June 2023

ACCEPTED FOR PUBLICATION
10 July 2023

PUBLISHED
20 July 2023

MADE OPEN ACCESS
21 August 2023

PAPER

Chiral single photons from deterministic quantum emitter arrays via proximity coupling to van der Waals ferromagnets

Na Liu[1,3], Licheng Xiao[1,3], Shichen Fu[2,3], Yichen Ma[1,3], Song Liu[4], Siwei Chen[2,3], James Hone[4], Eui-Hyeok Yang[1,3] and Stefan Strauf[1,3,*]

[1] Department of Physics, Stevens Institute of Technology, Hoboken, NJ 07030, United States of America
[2] Department of Mechanical Engineering, Stevens Institute of Technology, Hoboken, NJ 07030, United States of America
[3] Center for Quantum Science and Engineering, Stevens Institute of Technology, Hoboken, NJ 07030, United States of America
[4] Department of Mechanical Engineering, Columbia University, New York, NY 10027, United States of America
[*] Author to whom any correspondence should be addressed.

E-mail: sstrauf@stevens.edu

Keywords: quantum emitter, chiral, WSe_2, nonreciprocal, proximity coupling, MoS_2, ferromagnetic

Supplementary material for this article is available online

Abstract

Chiral single photons are highly sought to enhance encoding capacities or enable propagation-dependent routing in nonreciprocal devices. Unfortunately, most semiconductor quantum emitters (QEs) produce only linear polarized photons unless external magnets are applied. Magnetic proximity coupling utilizing 2D ferromagnets promises to make bulky external fields obsolete. Here we directly grow Fe-doped MoS_2 (Fe:MoS_2) via chemical vapor deposition that displays pronounced hard ferromagnetic properties even in monolayer form. This approach with monolayer ferromagnets enables full utilization of the strain from the pillar stressor to form QE in WSe_2 deterministically. The Fe:MoS_2/WSe_2 heterostructures display strong hysteretic magneto-response and high-purity chiral single photons with a circular polarization degree of $92 \pm 1\%$ (74% average) without external magnetic fields. Furthermore, the chiral single photons are robust against uncontrolled twist-angle and external stray-fields. This ability to manipulate quantum states and transform linear polarized photons into high-purity chiral photons on-chip enables nonreciprocal device integration in quantum photonics.

1. Introduction

Combining the chirality of light with single-photon emission has created a new forefront of research in quantum optics [1]. Optical chirality, classified by right-(σ^+) and left-(σ^-) circular polarization, provides advances in encoding capacities in quantum information [2–4] and quantum computing [5–7]. The chirality also enables propagation-dependent routing, i.e., nonreciprocity through time-reversal symmetry breaking [8]. One way to generate optical chirality of single photons is by integrating single photon emitters with spin-polarizing devices like ring resonators or nanobeam waveguides [9]. For example, we have shown recently that the time-reversal symmetry breaking in ring resonators combined with spin–orbit locking provides a twisted single photon source [10]. Often such kind of realizations needs a strong magnetic field either to tune the emission [11] or to lift the degeneracy of quantum dots [12], which is hard to scale in on-chip technologies. Thus, it would be of great interest if chirality could be achieved without an external field. To this end, 2D materials such as transition metal dichalcogenides (TMDCs) offer outstanding optical, mechanical, and magnetic properties for on-chip integration.

Specifically, TMDC monolayers feature strong spin-orbit coupling and intrinsic inversion symmetry breaking, resulting in valley degeneracy at the K and K' points in the conduction band [13, 14]. The valleytronic effects can be probed through the circularly polarized light emission of 2D excitons (ensemble emission) [15]. Optical valley initialization is based on chiral selection rules for band-to-band transitions: σ^+ polarized excitation results in the transition in the K valley, and correspondingly σ^- polarized excitation results in the transition in the K' valley [15, 16]. Experimental confirmation of circularly polarized

light has been reported in photoluminescence (PL) measurements in Mo-based TMDCs [17–19] and W-based TMDCs [13, 20–22]. By coupling to plasmonic gap-mode nanocavities, the degree of circular polarization (DOP) for 2D exciton emission from WSe_2 can reach almost unity (99%) [23]. Furthermore, when TMDCs form heterostructures with van der Waals ferromagnets, pronounced magnetic proximity coupling can occur and create novel magneto-optical and electrical properties [24]. The proximity coupling was recently demonstrated via spin-valley polarization light signatures in the optical response of 2D neutral excitons residing in EuS/WSe_2 [25], $EuO/MoTe_2$ [26], and CrI_3/WSe_2 [27, 28]. However, this high purity of optical chirality is achieved through classical light emission from the exciton ensemble in TMDCs, but not at the level of single photons, i.e., not for quantum light.

In contrast, for quantum light emission from individual excitons confined to 0D potentials in WSe_2, the chirality is typically absent since the underlying strain anisotropy splits the exciton states into two linear polarized transitions [29–32]. The loss of chirality can be restored by applying a magnetic field from external superconducting coils, resulting in the gradual change from linear polarization to the ideal circular polarization required for quantum information processing [33–35]. This behavior is typically observed regardless of the specific technique utilized to produce strain-induced 0D confinement potentials, including randomly distributed nanobubbles [36, 37], spatially deterministic pillars [38], nanogaps [34], nanostars [39] or via atomic force microscope (AFM) indentation on top of transferred monolayers [40]. One way to potentially overcome the anisotropy without using external magnetic fields is to design heterostructures that benefit from on-chip magnetic proximity coupling from van der Waals ferromagnets. To this end, recent work on quantum emitters (QEs) in WSe_2 has demonstrated ultra-high g factor up to 20 ± 1 through coupling to soft ferromagnets $Cr_2Ge_2Te_6$ (CGT) [41]. The soft ferromagnetic nature, however, does not allow spin state manipulation in the absence of external fields since there is no remanence. Hard ferromagnets such as Fe_3GeTe_2 (FGT) do allow proximity-coupling to QE [42] and even the realization of localized charged excitons in 0D when using CrI_3 ferromagnets [43]. Unfortunately, these van der Waals materials display strongly reduced ferromagnetism with decreasing number of layers [44], while monolayer ferromagnets are necessary to create site-controlled QE through the stressor technique.

Here we overcome these limitations by utilizing our chemical vapor deposition (CVD)-grown Fe-doped MoS_2 (Fe:MoS_2) monolayers that show strong hard ferromagnetic properties even in monolayer form. When integrated into Fe:MoS_2/WSe_2 heterostructures, we demonstrate magnetic proximity coupling of site-controlled QE that generates chiral single photons with high purity up to $92 \pm 1\%$, even in the absence of external magnetic fields. Furthermore, our detailed analysis shows that the chiral photons are robust against uncontrolled external stray fields, making them particularly attractive for creating on-chip nonreciprocal quantum photonic devices.

2. Results

The goal is to achieve strong ferromagnetic proximity coupling from the strain-induced QE in WSe_2. To fully utilize the strain from the stressor on the substrate, 2D ferromagnets are required that are thin enough to transfer the strain through them within the heterostructure. To this end, FGT or CGT is not only notoriously difficult to exfoliate down to the monolayer level but displays strongly reduced ferromagnetism with decreasing number of layers [44]. To overcome these limitations, we use CVD growth of monolayer Fe:MoS_2, which is shown to be ferromagnetic even at room temperature [45]. Another advantage of using CVD-grown Fe:MoS_2 is that it can cover 1×1 mm^2 arrays entirely, which cannot be achieved through exfoliation techniques. This ability simplifies the layer assembly process. The sample configuration and top-down view of the assembled heterostructure of Fe:MoS_2/WSe_2 are shown in figures 1(a) and (b), respectively. The stack is fabricated using the dry-stamping technique on top of arrays consisting of 80 nm tall square-shaped gold pillars, covered with a 2 nm Al_2O_3 layer to avoid charging effects from the substrate. The pillar arrays are optically visible through multilayers of WSe_2, as can be seen in figure 1(b). Overall we recorded data from five Fe:MoS_2/WSe_2 heterostructures strained over nanopillar arrays with various relative orientation angles (see figure S1 and supplementary note1).

To further investigate the degree of strain for this Fe:MoS_2/WSe_2 heterostructure, we have compared the AFM image from the multilayer region, Fe:MoS_2/WSe_2 bilayer heterostructure, and bare Fe:MoS_2 monolayer, as highlighted in figure 1(c). It is evident in this AFM image that all nanopillars with a height of 80 nm remain intact after layer transfer. In addition, the Fe:MoS_2/WSe_2 heterostructure does not suffer from piercing over the pillars, as confirmed by scanning-electron microscope (SEM) imaging (see figure 2). To characterize the strain, we define the $\rho = \frac{\mathrm{FWHM}}{\mathrm{Height}}$, a relative measure that is proportional to the apex angle, where FWHM is the full width at half maximum, as highlighted by the arrows in the corresponding AFM line scans in figures 1(d)–(f). The ratio $\rho = 5.6$ is quite high for the multilayer WSe_2 region, indicating a large apex angle and, thus, low strain. The value of $\rho = 2.3$ for the Fe:MoS_2/WSe_2 heterostructure is close to the one for monolayer Fe:MoS_2

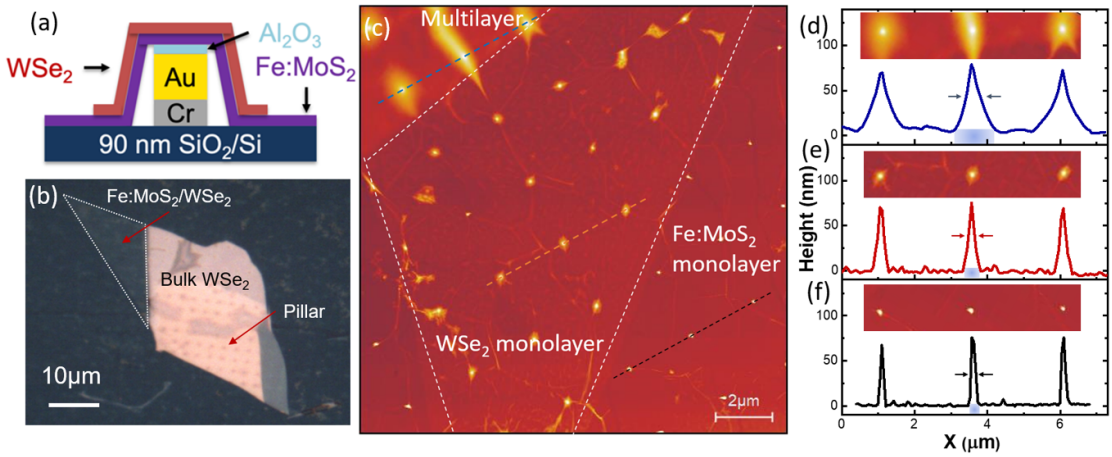

Figure 1. Formation of proximity-coupled quantum emitter arrays. (a) Cross section schematic of Fe:MoS_2/WSe_2 heterostructure strained over 80 nm tall Cr/Au nanopillars that are capped with 2 nm Al_2O_3. (b) Corresponding optical-microscope image of an assembled Fe:MoS_2/WSe_2 heterostructure on a nanopillar array. The white dotted lines highlight the intersection of the heterostructure area. The highly reflective area in the center is the multilayer (bulk) region of WSe_2 adjacent to the monolayer. (c) Corresponding AFM image of the triangular heterostructure area. (d) AFM line scan from the multilayer area following the blue dotted line in (c). (e) Comparable line scan for the Fe:MoS_2/WSe_2 heterostructure (yellow dashed line in (c)). (f) Line scan for Fe:MoS_2 monolayer (black dashed line). The arrows in each figure (d), (e) points the full width at half maximum (FWHM) linewidth and the blue area is the layer bending width on top of pillars. The top insets in (d)–(f) are the cropped AFM images from (c) for comparison.

of $\rho = 1.7$, implying significantly lower apex angles and thus larger strain into the 2D materials. This strain localized to the apex region is known to create localization of the 2D excitons into 0D confinement potentials, thereby forming strain-induced QE in the van der Waals materials [37, 38].

Room temperature PL spectra of the Fe:MoS_2/WSe_2 heterostructure are characterized by two prominent transitions at 1.6 eV and 1.83 eV, that correspond to the 2D neutral exciton emission from the WSe_2 and Fe:MoS_2 monolayers, respectively (figure 2(a)). Upon cooling to 3.8 K, additional transition lines appear predominantly from WSe_2, including the 2D neutral excitons (X^0) at 1.73 eV, the dark exciton (X^D) at 1.68 eV, the broad defect band exciton occurring in the area from 1.65 eV to 1.7 eV, as well as several spectrally sharp lines corresponding to strain-induced 0D QE (figure 2(b)). These transitions are identified in accordance with our previous reports of PL from monolayer WSe_2 [42, 46] and strain-induced pillars showing on average four QE lines per cubic pillar location [38]. Recording the antibunching nature through the second-order time correlation function reveals $g^{(2)}(\tau = 0) = 0.10 \pm 0.05$ under pulsed excitation, i.e. high-purity triggered single photon emission from these strain-induced QE (see figure S3), in agreement with our previous findings that every sharp line behaves as a single QE [38]. In the following, we focus our study on those QE that appear spectrally well separated from the broad emission bands on the low energy side in the spectrum (see blue arrow in figure 2(b)), in order to avoid detrimental overlap with other transitions. A characteristic feature of these QE is their fine structure splitting (FSS) at zero magnetic fields. All investigated QE display spectral doublets when recorded with high spectral resolution with a typical FSS energy $\Delta_0 = 500$–800 μeV [41]. To investigate the magneto-PL properties of each QE, we applied the magnetic field parallel to the k vector of the incident laser. Figure 2(c) shows the splitting behavior as a function of the magnetic field for a QE with a Δ_0 of 630 μeV, which originates from the electron–hole spin exchange interaction as well as the underlying anisotropic strain [31, 33]. With increasing magnetic field, the two components of the clearly resolved Zeeman doublet split further apart, while the low-energy peak becomes dominant due to thermalization (figure 2(c)).

In our previous work, we have shown that Fe-related hard van der Waals magnets such as Fe_3GeTe have magnetization ranges from 1.2 to 1.8 μ_B, giving rise to a pronounced hysteresis loop of the QE in an Fe_3GeTe/WSe_2 heterostructure [42]. It is not *a priori* clear if CVD-grown dilute magnetic semiconductors (DMSs) such as the Fe-doped MoS_2 monolayers utilized in this study can also show proximity-coupling to exciton-based QE, given that the atomic concentration of substitutional Fe atoms is only about 0.5%. Nonetheless, our Fe:MoS_2 monolayers are characterized by strong ferromagnetic hysteresis in the magnetization, as determined in superconducting quantum interference device measurements, as well as pronounced hysteresis loops in the magnetic circular dichroism [45]. The ferromagnetic response of monolayer Fe:MoS_2 makes magnetic proximity coupling highly likely when interfaced in direct contact with QE in WSe_2. As a first signature, we show that pronounced exciton g-factor enhancement occurs for QE within the heterostructures. We have recorded the g-factors (see figure 4) for ten QE

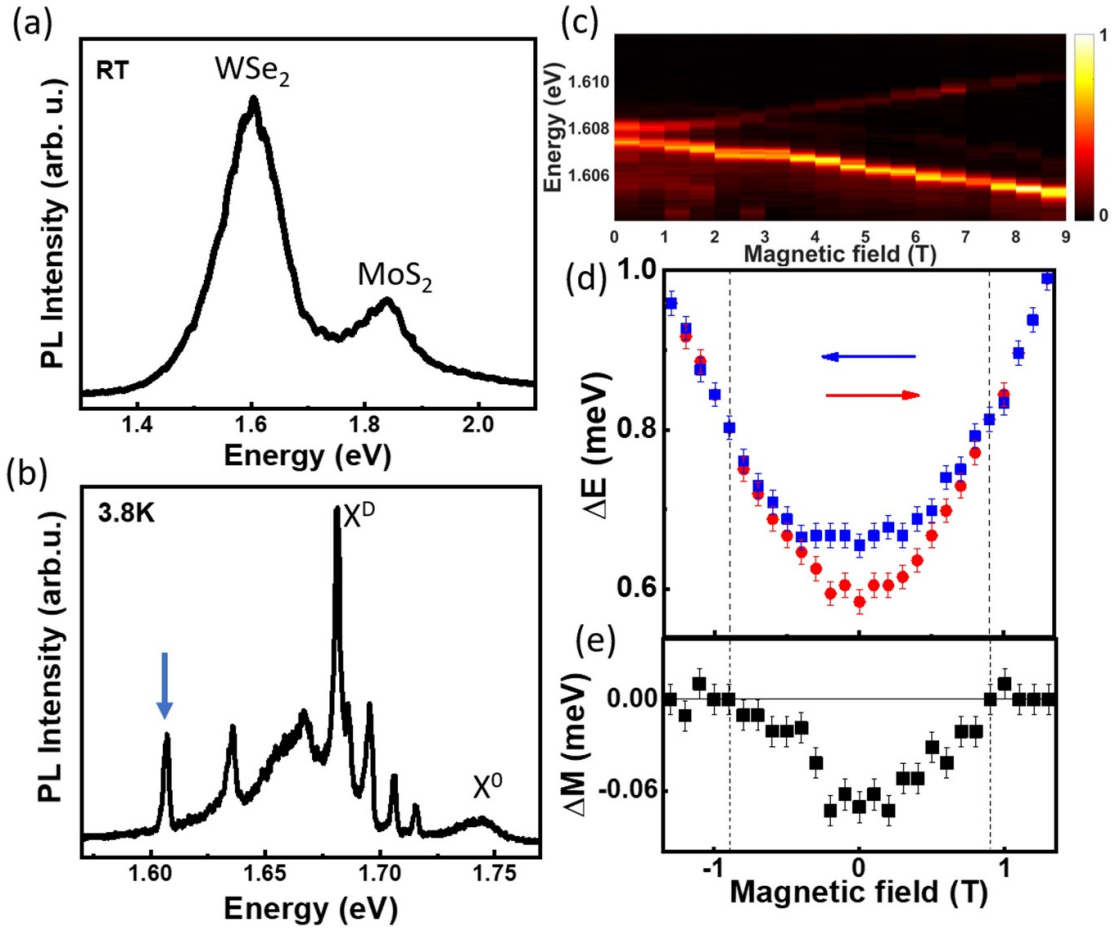

Figure 2. Magneto-optical characterization of proximity-coupled quantum emitters. (a) Photoluminescence spectrum of Fe:MoS_2/WSe_2 heterostructure measured at room temperature (RT). (b) PL spectrum of the heterostructure recorded at 3.8 K and spectrally zoomed in for the WSe_2 emission (b). The blue arrow highlights a deeply localized (0D) quantum emitter. X^0: neutral 2D exciton, X^D: dark 2D exciton transition (c) Corresponding Zeeman-doublet pattern of the highlighted quantum emitter at 1.608 eV. (d) Zeeman energy splitting value ΔE as a function of increasing (red circle) and decreasing (blue square) magnetic field sweep direction. (e) Extracted energy difference ΔM between the red and blue curves characterizing the hysteretic response of the quantum emitter. All data in (c)–(e) are recorded at 3.8 K.

located in bare flux-grown WSe_2 monolayers and 11 QE located in various Fe: MoS_2/WSe_2 heterostructures and found that the average value changes from $g = 5.6$ in bare WSe_2 QE to $g = 9.7$ in Fe:MoS_2/WSe_2, which is 1.73 times enhanced by the magnetic proximity coupling (see figure 5). In addition, we observe pronounced ferromagnetic hysteresis loops for the QE emission from the Fe:MoS_2/WSe_2 heterostructure when sweeping the magnetic field, as shown in figure 2(d). The red circles correspond to the increasing magnetic field and blue square correspond to decreasing magnetic field sweep direction. The ferromagnetic coupling strength can be quantified from the swing ΔM defined as the difference between the decreasing value and increasing value of ΔE in the hysteresis loop (figure 2(d)). Similar behavior was observed for eight different QE on the nanopillar arrays with ΔM values ranging from 20–72 μeV (figure S6). This demonstrates that the ferromagnetic proximity-coupling can be reliably observed also for DMS, albeit with a three-fold local variation in coupling strength. The variation is likely caused by spatial nonuniformity of the ferromagnetic field and the varying direction of dipole momentum of the QE within the heterostructure. As a result, our all-optical read-out technique can sense the magnetic proximity field from a DMS through spatially deterministic QE arrays in Fe:MoS_2/WSe_2 heterostructures.

Towards demonstrating chiral single photons in the absence of external magnetic fields, we show in figure 3 first the comparison study with a bare WSe_2 monolayer on top of the nanopillar arrays. The characteristic signature of strain-induced QE in the bare WSe_2 monolayer is their high degree of linear polarization response of the fine structure doublet at 0 T external magnetic field [35], which is even maintained under electroluminescence [31]. Figures 3(a)–(c) show the polarization analysis for a QE centered at 1.644 eV. The spectral doublet of the QE shows a pronounced polarization behavior under probing with linear polarizers with a periodicity of 180° (figure 3(a)). The corresponding spectra in figure 3(b) highlight the complete spectral separation in the form of horizontal (H: red trace) and

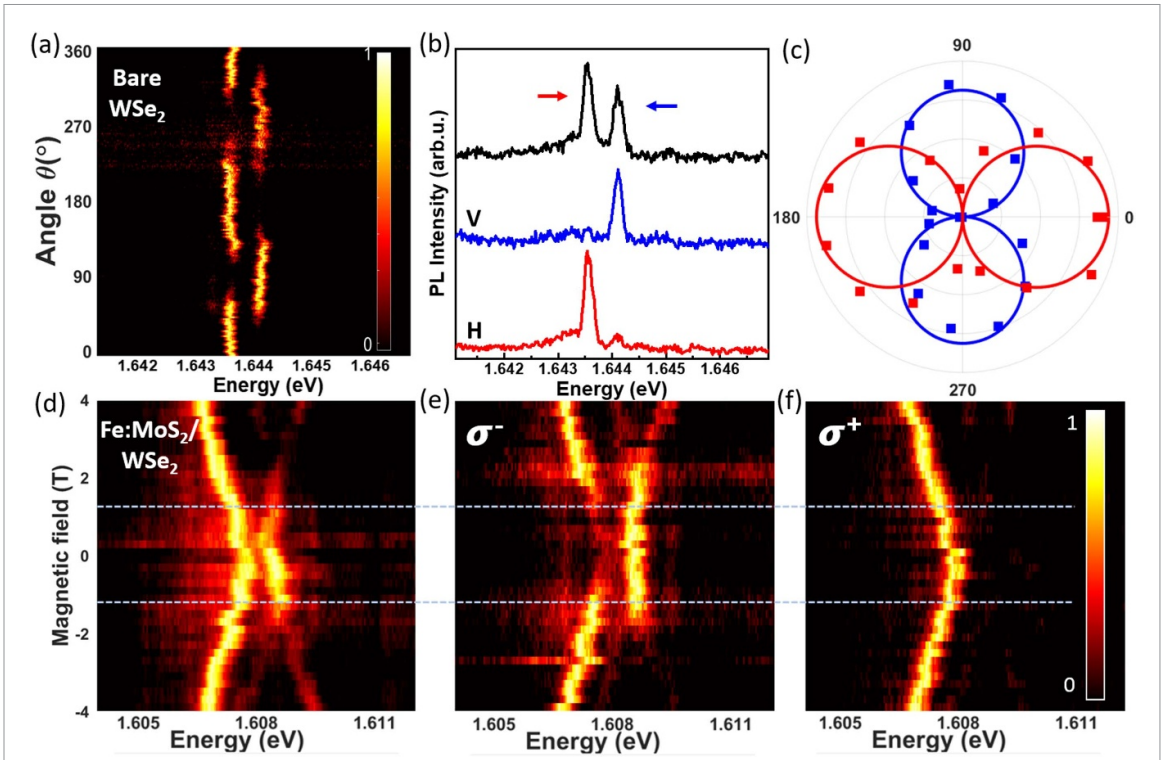

Figure 3. Comparison of quantum emitter polarization dependence between monolayer WSe_2 (bare) and Fe:MoS_2/WSe_2 heterostructures. (a) Optical spectra recorded without applied field (0 T) and plotted as a function of linear-polarizer detection angle for a strain-induced quantum emitter in monolayer WSe_2, i.e., without magnetic proximity coupling. (b) Corresponding selective PL spectra without polarizer (black line, unpolarized), with linear polarizer set at 95° (blue line, V-polarized) and 5° (red line, H-polarized). (c) Polar plot of QE emission intensity for H and V-polarized transitions of the Zeeman doublet. (d) Magnetic-field dependence of Zeeman pattern for the magnetic proximity-coupled quantum emitter at 1.608 eV in the Fe:MoS_2/WSe_2 heterostructures recorded without a polarizer in the detection path. (e), (f) Same but recorded with left-circular polarizer σ^- (e) and right-circular polarizer σ^+ (f) in the detection path. All spectra are normalized to unity (yellow color) and were recorded at 3.8 K.

vertical (V: blue trace) linear polarization states, as extracted from the data in figure 3(a) at polarizer settings of $\theta_0 = 5°$ and 95°, respectively. Following Wang *et al* [35], we use $I = I_0 + b\sin\frac{\pi(\theta-\theta_0)}{a}$ to fit the integrated PL intensity of two orthogonal components in figure 3(c), which follows from Malus $\cos^2$ law and the half-angle formula. The degree of linear polarization can be quantified by using the expression $\eta = \frac{I_H - I_V}{I_H + I_V}$, where I_H and I_V are the PL intensities of the H and V transitions. The extracted values of $\eta = 90 \pm 2\%$ and $95 \pm 2\%$ for the H- and V-polarized FSS states, respectively, demonstrate the high degree of linear polarization achieved with strain-induced QE in WSe_2. In contrast, for the magnetic proximity-coupled heterostructure, the FFS states are found to be circularly polarized. Figures 3(d)–(f) show the magnetic-field dependence of the Zeeman pattern for the proximity-coupled QE at 1.608 eV in the Fe:MoS_2/WSe_2 heterostructures recorded without a polarizer (figure 3(d)), with a left-circular polarizer σ^- (figure 3(e)) and a right-circular polarizer σ^+ (figure 3(f)) in the detection path. When focusing on the highlighted magnetic field region below ± 1.5 T (see horizontal dashed lines), that is, before the intensity of the high energy component quenches, pronounced circularly polarized states are observed (figures 3(e) and (f)) even down to zero externally applied field. Comparable behavior has been found in detailed polarization studies of four additional QE within Fe:MoS_2/WSe_2 heterostructures (see figure S7). To exclude interface phenomena, we have carried out another control experiment where we have grown MoS_2 without offering Fe during growth, otherwise created the exact same heterostructures strained over nanopillar stressors. In the absence of ferromagnetism there is no magnetic proximity-coupling, and as a result the optical emission remains linearly polarized, with no sign of hysteresis ($\Delta M = 0$), and no sign of chiral single photon emission (see figure S8). Therefore, this change from linear to circular polarization for the QE emission results from the magnetic proximity coupling mediated by the strong remanent magnetization of the Fe-doped MoS_2 monolayer.

To further analyze the DOP and the thermalization behavior of the QE intensity, we show the individual PL spectra recorded under σ^- (red line) and σ^+ (blue line) polarizationdetection for nine representative magnetic field values in figure 4(a). At zero field, the FSS states have equal intensity (oscillator strength) and are fully spectrally separated. Under σ^- probing, the intensity of the high energy component

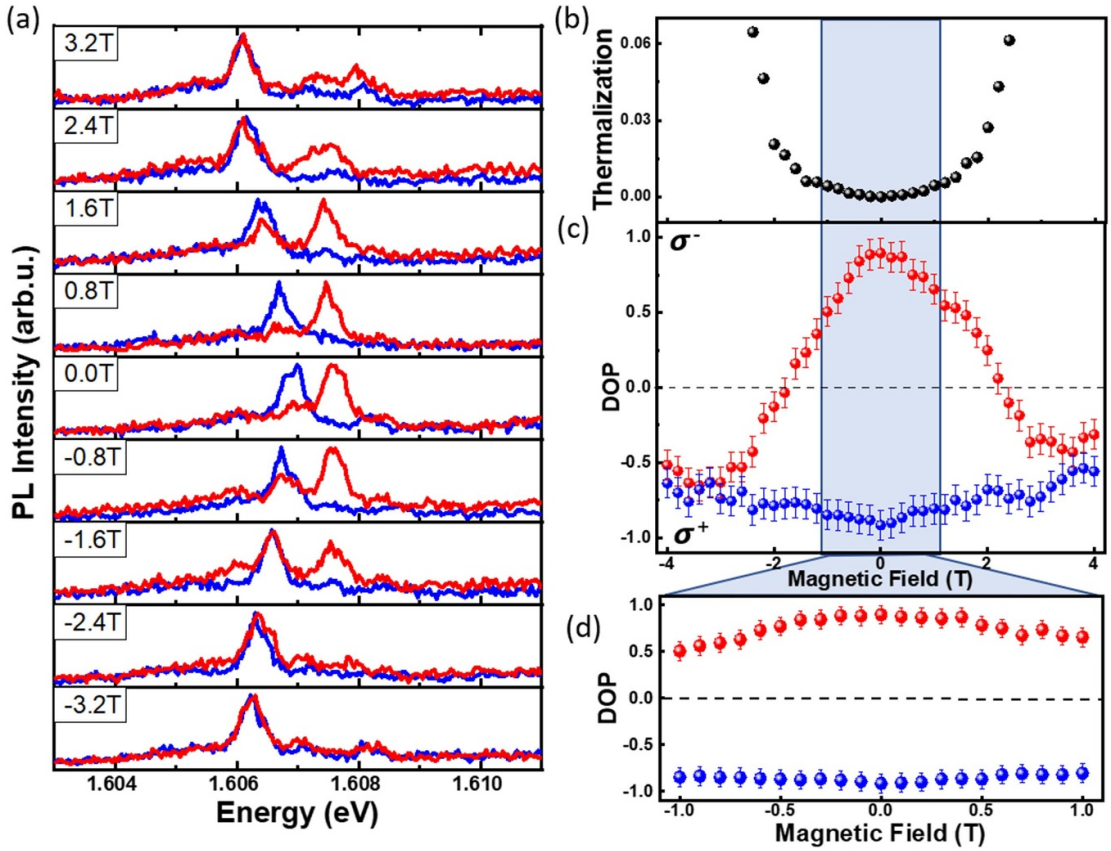

Figure 4. Signature of chiral quantum light emission under magnetic proximity coupling. (a) Spectral overlay of PL spectra recorded for two orthogonal circular polarizer settings, σ^- (red line) and σ^+ (blue line), plotted for nine representative magnetic field values. (b) State thermalization factor according to $\exp(-\Delta E/kT)$ with ΔE corresponding to the measured Zeeman splitting energy at each magnetic field value. (c) Degree of circular polarization (DOP) as a function of applied magnetic field for the high energy spin component (σ^- polarized, red) and low-energy spin component (σ^+-polarized, blue). (d) Fine-sweep of circular DOP for the blue-shaded region in (b), (c) where the quantum emitter spin state thermalization is minimized. All data recorded at 3.8 K.

is first stable with an increasing magnetic field, but then starts to quench drastically above about 2 T. At high magnetic fields, the intensity of the low energy component dominates the spectrum regardless of the polarization state. This behavior is typical for a two-level system that undergoes thermalization. In this case, the intensity ratio I_H/I_L, where I_H (I_L) is the PL intensity of the high energy peak (low energy peak), is proportional to $\exp(-\Delta E/k_BT)$, where ΔE corresponds to the measured Zeeman splitting energy at each magnetic field value and $k_BT = 0.32$ meV at 3.8 K. This thermalization behavior shown in figure 4(b) normalized to the intensity ratio at 9 T. The DOP can be defined as $\mathrm{DOP} = \frac{I_{\sigma-} - I_{\sigma+}}{I_{\sigma-} + I_{\sigma+}}$, where $I_{\sigma-}$ is the intensity of the high energy spin component (σ^- polarized, red) and $I_{\sigma+}$ is the intensity of the low-energy spin component (σ^+-polarized, blue). Figure 4(c) shows an overview of the DOP of the QE versus the magnetic field in the quenching regime. With increasing Zeeman splitting energy, as apparent from figure 4(b), the intensity of the energetically higher components almost vanishes, giving rise to a sharp drop of the DOP towards -1 in the ideal case, i.e., a dominant chiral photon emission with right circular polarization σ^+. The actual values settle in around $\mathrm{DOP} = -0.6 \pm 0.1$ due to nonvanishing background emission. Figure 4(d) shows a zoom into the low field regime where the circular polarization states are well-defined, and thermalization effects are minimal, as highlighted by the blue area. In this regime, the DOP reaches very high values, with an average value of 88 ± 1% for σ^- and 85 ± 1% for σ^+ in the magnetic field range from −0.5 T to 0.5 T, as well as a maximum value of 92 ± 1% and 90 ± 1% for σ^- and σ^+ at zero external fields, respectively. Lastly, we have recorded zero-field DOP values for nine QE located in five different Fe:MoS_2/WSe_2 heterostructures with various relative orientations between the monolayers (see supplementary note 1). All QE depicted in figure 5 show chiral single photon emission with high average DOP values of 74.2 ± 1% for σ^- and 73.9 ± 1% for σ^+, respectively. No pronounced effect of twist angle is observed, as expected for these strain-induced QE excitons that remain localized within the monolayer of WSe_2 (intralayer excitons) and emit in the range from 1.55 to 1.72 eV. The corresponding interlayer excitons in MoS_2/WSe_2 heterostructures which are sensitive to the twist angle emit strongly red

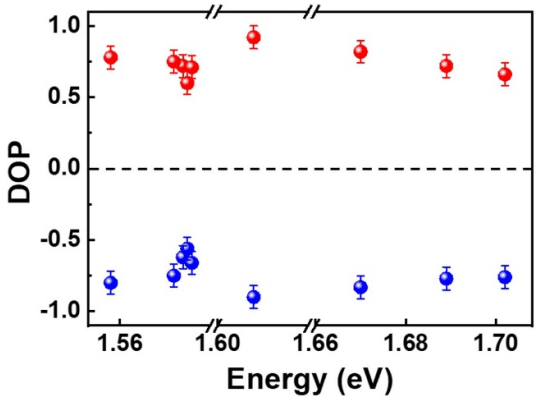

Figure 5. Zero-field DOP values recorded for nine QE located in five different Fe:MoS_2/WSe_2 heterostructure samples. The red circles are for σ^- polarized and the blue circles for σ^+ polarized component of the Zeeman doublet.

shifted down to 0.96–1.05 eV (1180–1280 nm) [46], i.e., outside of our observation window. The data demonstrate that high-purity chiral single photons are created through the magnetic proximity coupling to CVD-grown monolayer Fe:MoS_2, even without an external magnetic field. Furthermore, our chiral QE system is robust against uncontrolled rotations in the heterostructure as well as external magnetic stray-fields, such as earth's magnetic field, maintaining a high DOP, as required for practical applications in quantum information science.

In Conclusion, we have achieved strong ferromagnetic proximity coupling from strain-induced QE in WSe_2 by utilizing CVD-grown monolayer Fe:MoS_2. This approach has overcome difficulties with the exfoliation of bulk van der Waals ferromagnets such as FGT and enabled us to fully utilize the strain from the stressor on the substrate when forming proximity-coupled 0D QE deterministically. We have shown that QEs in bare WSe_2 are characterized by a near unity degree of linear polarization. In contrast, the resulting Fe:MoS_2/WSe_2 heterostructures display strong hysteretic magneto-response in the exciton emission with a high-purity of chiral single photons as characterized by a circular polarization degree up to 92 $\pm$ 1%. As a key finding, we have demonstrated chiral single photon generation directly on-chip and in the absence of an external magnetic field, thereby eliminating the need for superconducting coils to generate chiral quantum light. Furthermore, the chiral photons are robust against uncontrolled twist angles and external stray fields. This ability to manipulate quantum states and transform linear polarized photons to chiral photons directly on chip via magnetic proximity coupling enables device miniaturization for tasks in quantum photonics. The time-reversal symmetry breaking that can be achieved with high-purity chiral single photons is of particular interest due to their robustness against noisy backgrounds and might enable to engineer nonreciprocal photonic devices, including single-photon circulators and isolators in future applications.

3. Methods

3.1. Pillar array substrate fabrication

The pillar arrays were patterned by electron-beam lithography (EBL) using 495 Poly (methyl methacrylate) (PMMA) A4 (MicroChem) that was spin-coated at 2000 rpm onto the SiO_2 substrate. The side lengths of the individual cubes were defined to be 110 nm, with a height of 80 nm. The samples were subsequently patterned by an Elionix ELS-G100 EBL system and developed in MIBK: IPA 1:3 for 5 min. To convert the polymer template into a plasmonic array we deposited a 10 nm Cr adhesion layer and 70 nm Au metal on the chip in an electron beam evaporator (AJA Orion 3-TH) followed by liftoff in warm Acetone at 50 °C. Finally, a 2 nm thick layer of Al_2O_3 was deposited by atomic layer deposition (Ultratech Fiji G2) [38].

3.2 Flux-growth of WSe_2

crystals were synthesized by reacting W powder, 99.999%, with Se shot, 99.999%, typically in a ratio of 1:20. These materials were first loaded into a quartz ampoule with a quartz wool for decanting, then evacuated and sealed at $\sim 10^{-3}$ Torr. For growth, the ampoule is heated to 1000 °C over 48 h, held for 3 d, then cooled at 1.5 °C hr^{-1} to 400 °C and subsequently flipped and centrifuged. Crystals are then annealed at 250 °C with the cold end of the quartz ampoule held at 100 °C for 48 h [47, 48].

3.3 Synthesis of monolayer Fe:MoS_2

Fe:MoS_2 monolayers were grown by CVD onto a SiO_2/Si substrate. The Fe doping was achieved during MoS_2 growth process by incorporating Fe_3O_4 particles. Fe_3O_4 particles were evenly cast onto the SiO_2/Si substrate before contacting the MoO_3-deposited substrate face-to-face. Before applying the particles, the substrate was washed using deionized (DI) water, followed by annealing at 110 °C for 5 min on a hot plate. For the growth, the furnace temperature was set at 850 °C with a ramping rate of 18 °C min^{-1}, and an argon gas (30 sccm) was supplied from 300 °C. Sulfur vapor was supplied when the furnace temperature reached 790 °C, and a hydrogen gas (15 sccm of) was delivered 1 min before Sulfur supplied. After the growth, a few hundred-micron sizes of monolayer Fe:MoS_2 were found on top of SiO_2/Si substrate [45]. To transfer Fe:MoS_2 monolayer on pillars, first, few drops of PMMA (950 K A4) was cast to cover the top of

SiO_2/Si substrate. The PMMA-covered sample was left in ambient condition for 2 h to make it cure. The PMMA/Fe:MoS_2/substrate was then floated in a 30% KOH solution at room temperature. The KOH solution will etch SiO_2 layer slightly, then rapidly separate PMMA/Fe:MoS_2 from the substrate. The PMMA/Fe:MoS_2 layer was then rinsed with 3 batches of DI water for 10 min each time [49]. After rinsing, the PMMA/Fe:MoS_2 was scooped using a clean PDMS sample with Fe:MoS_2 facing up. Next, an air blower was used to blow water from the PMMA layer, and PMMA/Fe:MoS_2 was put in a vacuum chamber for another 10 min. The PDMS/PMMA/Fe:MoS_2 was attached under a glass slide and held by an *xyz*-movable micromanipulator for aligned transfer. Once the area with nanopillars was identified under the microscope, the PMMA/Fe:MoS_2 was transferred on top of the pillar substrate through the hot transfer technique [36].

3.4 WSe_2 exfoliation and transfer

Monolayers of WSe_2 were exfoliated from bulk crystals grown by the flux-growth technique, giving rise to a one to two orders of magnitude lower defect density and a higher emission PL intensity, as we previously reported [41]. For layer transfer we followed our previous dry hot-stamping procedure utilizing an elevated substrate temperature of 60 °C to prevent nanobubble formation [36]. Between each stamping transfer process, we followed thermal annealing at 350 °C for 12 h to achieve clean interfaces.

3.5 Optical measurements

PL measurements were performed at 3.8 K using a closed-cycle cryogen-free cryostat (attoDRY 1100, attocube systems AG). For optical excitation, we used a laser diode operating at 532 nm in continuous-wave mode. A laser spot size of ∼0.85 μm was achieved using a cryogenic microscope objective with a numerical aperture of 0.82. The relative position between the sample and the laser spot was adjusted with a cryogenic piezoelectric *xyz* stepper, whereas 2D scanned images were recorded with a cryogenic 2D-piezo scanner (Attocube). The spectral emission from the sample was collected in a multimode fiber, dispersed using a 0.75 m focal length spectrometer with either a 300 or 1200 groove grating, and imaged by a liquid nitrogen-cooled silicon charge coupled device camera. Magnetic fields were applied perpendicular to the plane of the sample within the range of −9 T to +9 T. Linear polarization-resolved PL measurements were performed by a combining a half-wave ($\lambda/2$) plate and a linear polarizer in the collection path. Circular polarization-resolved PL data were acquired by employing a quarter-wave ($\lambda/4$) plate and a linear polarizer in the collection path.

3.6 AFM imaging

The AFM measurements were obtained using a Bruker Dimension FastScan AFM in noncontact mode at a scan rate of 1.3 Hz with a FastScan-B tip. The AFM high profiles were extracted from the images using Gwyddion open-source software.

Data availability statement

The data cannot be made publicly available upon publication because they are not available in a format that is sufficiently accessible or reusable by other researchers. The data that support the findings of this study are available upon reasonable request from the authors.

Acknowledgments

Primary support for this work was provided by the National Science Foundation (NSF) under award DMR-1809235 (Stevens Institute of Technology) and DMR-1809361 (Columbia University). Synthesis of flux WSe_2 crystals was supported by the NSF MRSEC program through Columbia in the Center for Precision Assembly of Superstratic and Superatomic Solids (DMR-1420634).

ORCID iDs

Eui-Hyeok Yang https://orcid.org/0000-0003-4893-1691
Stefan Strauf https://orcid.org/0000-0002-9887-7059

References

[1] Chen D, He R, Cai H, Liu X and Gao W 2021 Chiral single-photon generators *ACS Nano* **15** 1912–6
[2] Wang J *et al* 2012 Terabit free-space data transmission employing orbital angular momentum multiplexing *Nat. Photon.* **6** 488–96
[3] Petersen J, Volz J and Rauschenbeutel A 2014 Chiral nanophotonic waveguide interface based on spin-orbit interaction of light *Science* **346** 67–71
[4] Xiao S *et al* 2021 Chiral photonic circuits for deterministic spin transfer *Laser Photon. Rev.* **15** 2100009
[5] Togan E *et al* 2010 Quantum entanglement between an optical photon and a solid-state spin qubit *Nature* **466** 730–4
[6] Basiri A, Chen X, Bai J, Amrollahi P, Carpenter J, Holman Z, Wang C and Yao Y 2019 Nature-inspired chiral metasurfaces for circular polarization detection and full-Stokes polarimetric measurements *Light: Sci. Appl.* **8** 78
[7] Kan Y H, Zhao C Y, Andersen S K H, Ding F, Kumar S and Bozhevolnyi S I 2020 Metasurface-enabled generation of circularly polarized single photons *Adv. Mater.* **32** 1907832
[8] Lodahl P, Mahmoodian S, Stobbe S, Rauschenbeutel A, Schneeweiss P, Volz J, Pichler H and Zoller P 2017 Chiral quantum optics *Nature* **541** 473–80
[9] Mahmoodian S, Lodahl P and Sørensen A S 2016 Quantum networks with chiral-light-matter interaction in waveguides *Phys. Rev. Lett.* **117** 240501
[10] Ma Y, Zhao H, Liu N, Gao Z, Mohajerani S S, Xiao L, Hone J, Feng L and Strauf S 2022 On-chip spin-orbit locking of

quantum emitters in 2D materials for chiral emission *Optica* **9** 953–8
[11] Brotons-Gisbert M, Branny A, Kumar S, Picard R, Proux R, Gray M, Burch K S, Watanabe K, Taniguchi T and Gerardot B D 2019 Coulomb blockade in an atomically thin quantum dot coupled to a tunable Fermi reservoir *Nat. Nanotechnol.* **14** 442–6
[12] Bayer M *et al* 2002 Fine structure of neutral and charged excitons in self-assembled In(Ga)As/(Al)GaAs quantum dots *Phys. Rev.* B **65** 195315
[13] Aivazian G, Gong Z, Jones A M, Chu R L, Yan J, Mandrus D G, Zhang C, Cobden D, Yao W and Xu X 2015 Magnetic control of valley pseudospin in monolayer WSe_2 *Nat. Phys.* **11** 148–52
[14] Macneill D, Heikes C, Mak K F, Anderson Z, Kormányos A, Zólyomi V, Park J and Ralph D C 2015 Breaking of valley degeneracy by magnetic field in monolayer $MoSe_2$ *Phys. Rev. Lett.* **114** 037401
[15] Cao T *et al* 2012 Valley-selective circular dichroism of monolayer molybdenum disulphide *Nat. Commun.* **3** 887
[16] Xiao D, Liu B G, Feng W, Xu X and Yao W 2012 Coupled spin and valley physics in monolayers of MoS_2 and other group-VI dichalcogenides *Phys. Rev. Lett.* **108** 196802
[17] Mak K F, He K, Shan J and Heinz T F 2012 Control of valley polarization in monolayer MoS_2 by optical helicity *Nat. Nanotechnol.* **7** 494–8
[18] Sallen G *et al* 2012 Robust optical emission polarization in MoS_2 monolayers through selective valley excitation *Phys. Rev.* B **86** 081301
[19] Zeng H, Dai J, Yao W, Xiao D and Cui X 2012 Valley polarization in MoS_2 monolayers by optical pumping *Nat. Nanotechnol.* **7** 490–3
[20] Jones A M *et al* 2013 Optical generation of excitonic valley coherence in monolayer WSe_2 *Nat. Nanotechnol.* **8** 634–8
[21] Kim J, Hong X, Jin C, Shi S F, Chang C Y S, Chiu M H, Li L J and Wang F 2014 Ultrafast generation of pseudo-magnetic field for valley excitons in WSe_2 monolayers *Science* **346** 1205–8
[22] Sie E J, McLver J W, Lee Y H, Fu L, Kong J and Gedik N 2014 Valley-selective optical Stark effect in monolayer WS_2 *Nat. Mater.* **14** 290–4
[23] Zhu G, Shi X, Huang G, Liu K, Wei W, Guo Q, Du W and Wang T 2022 Highly polarized light emission of monolayer WSe_2 coupled with gap-plasmon nanocavity *Adv. Opt. Mater.* **10** 2101762
[24] Burch K S, Mandrus D and Park J G 2018 Magnetism in two-dimensional van der Waals materials *Nature* **563** 47–52
[25] Zhao C *et al* 2017 Enhanced valley splitting in monolayer WSe_2 due to magnetic exchange field *Nat. Nanotechnol.* **12** 757–62
[26] Zhang Q, Yang S A, Mi W, Cheng Y and Schwingenschlögl U 2016 Large spin-valley polarization in monolayer $MoTe_2$ on top of EuO(111) *Adv. Mater.* **28** 959–66
[27] Zhong D *et al* 2017 Van der Waals engineering of ferromagnetic semiconductor heterostructures for spin and valleytronics *Sci. Adv.* **3** e1603113
[28] Seyler K L *et al* 2018 Valley manipulation by optically tuning the magnetic proximity effect in WSe_2/CrI_3 heterostructures *Nano Lett.* **18** 3823–8
[29] He Y M *et al* 2015 Single quantum emitters in monolayer semiconductors *Nat. Nanotechnol.* **10** 497–502
[30] Srivastava A, Sidler M, Allain A V, Lembke D S, Kis A and Imamoglu A 2015 Optically active quantum dots in monolayer WSe_2 *Nat. Nanotechnol.* **10** 491–6
[31] Kumar S, Kaczmarczyk A and Gerardot B D 2015 Strain-induced spatial and spectral isolation of quantum emitters in mono- and bilayer WSe_2 *Nano Lett.* **15** 7567–73
[32] Lu X, Chen X, Dubey S, Yao Q, Li W, Wang X, Xiong Q and Srivastava A 2019 Optical initialization of a single spin-valley in charged WSe_2 quantum dots *Nat. Nanotechnol.* **14** 426–31
[33] Linhart L, Paur M, Smejkal V, Burgdörfer J, Mueller T and Libisch F 2019 Localized intervalley defect excitons as single-photon emitters in WSe_2 *Phys. Rev. Lett.* **123** 146401
[34] So J P *et al* 2021 Polarization control of deterministic single-photon emitters in monolayer WSe_2 *Nano Lett.* **21** 1546–54
[35] Wang Q, Maisch J, Tang F, Zhao D, Yang S, Joos R, Portalupi S L, Michler P and Smet J H 2021 Highly polarized single photons from strain-induced quasi-1D localized excitons in WSe_2 *Nano Lett.* **21** 7175–82
[36] Shepard G D, Ajayi O A, Li X, Zhu X Y, Hone J and Strauf S 2017 Nanobubble induced formation of quantum emitters in monolayer semiconductors *2D Mater.* **4** 021019
[37] Darlington T P *et al* 2020 Imaging strain-localized excitons in nanoscale bubbles of monolayer WSe_2 at room temperature *Nat. Nanotechnol.* **15** 854–60
[38] Luo Y, Shepard G D, Ardelean J V, Rhodes D A, Kim B, Barmak K, Hone J C and Strauf S 2018 Deterministic coupling of site-controlled quantum emitters in monolayer WSe_2 to plasmonic nanocavities *Nat. Nanotechnol.* **13** 1137–42
[39] Peng L, Chan H, Choo P, Odom T W, Sankaranarayanan S K R S and Ma X 2020 Creation of single-photon emitters in WSe_2 monolayers using nanometer-sized gold tips *Nano Lett.* **20** 5866–72
[40] So J P *et al* 2021 Electrically driven strain-induced deterministic single-photon emitters in a van der Waals heterostructure *Sci. Adv.* **7** e3176
[41] Shayan K, Liu N, Cupo A, Ma Y, Luo Y, Meunier V and Strauf S 2019 Magnetic proximity coupling of quantum emitters in WSe_2 to van der Waals ferromagnets *Nano Lett.* **19** 7301–8
[42] Liu N, Gallaro C M, Shayan K, Mukherjee A, Kim B, Hone J, Vamivakas N and Strauf S 2021 Antiferromagnetic proximity coupling between semiconductor quantum emitters in WSe_2 and van der Waals ferromagnets *Nanoscale* **13** 832–41
[43] Mukherjee A, Shayan K, Li L, Shan J, Mak K F and Vamivakas A N 2020 Observation of site-controlled localized charged excitons in CrI_3/WSe_2 heterostructures *Nat. Commun.* **11** 5502
[44] Fei Z *et al* 2018 Two-dimensional itinerant ferromagnetism in atomically thin Fe_3GeTe_2 *Nat. Mater.* **17** 778–82
[45] Fu S *et al* 2020 Enabling room temperature ferromagnetism in monolayer MoS_2 via in situ iron-doping *Nat. Commun.* **11** 2034
[46] Karni O *et al* 2019 Infrared interlayer exciton emission in MoS_2/WSe_2 heterostructures 2019 *Phys. Rev. Lett.* **123** 247402
[47] Kim B *et al* 2022 Free trions with near-unity quantum yield in monolayer $MoSe_2$ *ACS Nano* **16** 140–7
[48] Edelberg D *et al* 2019 Approaching the intrinsic limit in transition metal diselenides via point defect control *Nano Lett.* **19** 4371–9
[49] Wang X, Kang K, Godin K, Fu S, Chen S and Yang E-H 2019 Effects of solvents and polymer on photoluminescence of transferred WS_2 monolayers *J. Vac. Sci. Technol.* B **37** 052902